

# Embedding planetesimals into white dwarf discs from large distances

Evgeni Grishin,<sup>1\*</sup> Dimitri Veras,<sup>2,3†</sup>

<sup>1</sup>*Technion, Israel Institute of Technology, Haifa, Israel, 3200003*

<sup>2</sup>*Centre for Exoplanets and Habitability, University of Warwick, Coventry CV4 7AL, UK*

<sup>3</sup>*Department of Physics, University of Warwick, Coventry CV4 7AL, UK*

12 August 2019

## ABSTRACT

The discovery of the intact minor planet embedded in the debris disc orbiting SDSS J1228+1040 raises questions about the dynamical history of the system. Further, the recent passage of the potentially interstellar object 1I/’Oumuamua within the solar system has reignited interest in minor body flux through exoplanetary systems. Here, we utilize the new analytical formalism from Grishin, Perets & Aveni (2019) to estimate the rate at which the gaseous components of typical white dwarf discs trap an exo-planetesimal. We compare the types of captured orbits which arise from planetesimals originating from the interstellar medium, exo-Kuiper belts and exo-Oort clouds. We find that the rate of interstellar medium injection is negligible, whereas capture of both exo-Kuiper and exo-Oort cloud planetesimals is viable, but strongly size-dependent. For a gaseous disc which extends much beyond its Roche limit, capture is more probable than disruption at the Roche limit. We find that the capture probability linearly increases with the radial extent of the disc. Even in systems without minor planets, capture of smaller bodies will change the disc size distribution and potentially its temporal variability. Our formalism is general enough to be applied to future discoveries of embedded planetesimals in white dwarf debris discs.

**Key words:** Planet-disc interactions – Oort Clouds – celestial mechanics – planets and satellites: dynamical evolution and stability – minor planets, asteroids: general – white dwarfs

## 1 INTRODUCTION

Exoplanetary science is no longer limited to the study of major planets alone. Their smaller cousins – exo-asteroids and exo-comets – play vital roles in understanding these systems, particularly after the host star has left the main sequence.

The broken-up remnants of exo-asteroids – easily seen in the photospheres of white dwarfs (WDs) – provide us with the most direct and abundant measurements of exoplanetary building blocks (Gänsicke et al. 2012; Jura & Young 2014; Harrison, Bonsor & Madhusudhan 2018; Hollands, Gänsicke & Koester 2018). These minor planets also reveal insights about planetary architectures, having been gravitationally perturbed towards the WD through a variety of dynamical mechanisms (Veras 2016). These mechanisms act in single-star systems with a single planet (Bonsor, Mustill & Wyatt 2011; Debes, Walsh & Stark 2012; Frewen & Hansen 2014) or multiple planets (Veras et al. 2016a; Mustill et al. 2018; Smallwood et al. 2018), which may or may not harbour moons (Payne et al. 2017). The presence of a stellar binary companion alone can trigger such perturbations, even without the presence of a

planet (Hamers & Portegies Zwart 2016; Petrovich & Muñoz 2017; Stephan, Naoz & Zuckerman 2017).

All types of planets which reach the WD phase must have survived engulfment from giant branch evolution. Two critical engulfment distances exist: one for the red giant branch phase (e.g. Villaver et al. 2014; Gallet et al. 2017; Rao et al. 2018; Sun et al. 2018) and another for the asymptotic giant branch phase (Mustill & Villaver 2012). Some treatments are general enough to determine the critical distances for both phases (Adams & Bloch 2013; Nordhaus & Spiegel 2013; Madappatt et al. 2016).

Before accreting onto a typical  $R_{\oplus}$ -sized WD, these minor planets will enter the star’s Roche, or disruption, radius, which extends out to about  $1R_{\odot}$ . Although direct infall onto the WD is possible, that target is small relative to its Roche radius. Hence, the much more likely outcome is the production of a debris disc (Graham et al. 1990; Jura 2003; Debes, Walsh & Stark 2012; Bear & Soker 2013; Veras et al. 2014a, 2015a). The size distribution which feeds the disc is unknown but may be constrained (Wyatt et al. 2014; Brown et al. 2017; Kenyon & Bromley 2017a,b). The compactness and other physical properties of these discs have been investigated in only a couple handfuls of investigations (Bochkarev & Rafikov 2011; Rafikov 2011a,b; Metzger, Rafikov & Bochkarev 2012; Rafikov & Garmilla 2012; Miranda & Rafikov 2018).

\* E-mail: eugeneg@campus.technion.ac.il (EG)

† STFC Ernest Rutherford Fellow

The theory of WD debris disc formation is borne out by observations. Of the over 40 discs known (Farihi 2016), about 20 per cent contain observable gas as well as dust (e.g. Gänsicke et al. 2006; Dennihy et al. 2018). We highlight three of these discs which have multi-epoch observations here: those orbiting SDSS J1228+1040, HE 1349-2305 and WD 1145+017. The structure of the first two can be deduced from their emission line profiles (Gänsicke et al. 2006; Manser et al. 2016, 2019), whereas the third is seen in absorption (Redfield et al. 2017; Cauley et al. 2018). These discs, with orbital periods of  $\approx 5$  hours, have been observed for about 1-10 years, and are suggestive of dynamically active systems.

In fact, individual exo-asteroids and smaller planetesimals or fragments have been observed in two of them. A single exo-asteroid has been observed to be distinegrating in real time for the last four years around WD 1145+017 (Vanderburg et al. 2015; Vanderburg & Rappaport 2018), shedding debris that contributes to the structure and evolution of the accompanying disc. A minor planet of a very different type that is consistent with a planetary core fragment has been detected orbiting SDSS J1288+1040 (Manser et al. 2019): this minor planet is embedded within the disc, at about  $0.73R_{\odot}$  – which is well within the canonical  $1R_{\odot}$  value – and does not feature observable ablation. Although no planetesimal has so far been discovered orbiting HE 1349-2305 (Dennihy et al. 2018), deeper observations are warranted.

These known exo-minor planets range in size from km-scale to hundreds of km (Rappaport et al. 2016; Veras, Marsh & Gänsicke 2016b; Gary et al. 2017; Gurri, Veras & Gänsicke 2017; Veras et al. 2017; Manser et al. 2019). However, many smaller fragments of unconstrained radii appear and disappear regularly in the photometric transit curves of the debris around WD 1145+017 (Vanderburg et al. 2015; Gänsicke et al. 2016; Rappaport et al. 2016; Izquierdo et al. 2018). Overall, planetesimals ranging in size of many orders of magnitude are either embedded within or just outside of WD discs.

However, despite their importance in exoplanetary science, these minor bodies still have murky dynamical histories. Even more challenging is the explanation of some of their current near-circular (Veras et al. 2017) or slightly or moderately eccentric orbits (Manser et al. 2019). In this paper, and inspired by the minor planet orbiting SDSS J1228+1040 and the recent passage of the interstellar interloper 1I/'Oumuamua through the solar system (Meech et al. 2017), we consider the probability of capturing interstellar and exo-planetesimals due to gas drag with a scaled-down gaseous disc.

Recently, Grishin, Perets & Avni (2019) showed that passing interstellar medium (ISM) planetesimals could be captured via aerodynamic gas drag in a protoplanetary disc. The number of 'Oumuamua-like planetesimals which are captured in a protoplanetary disc over its lifetime could be around  $10^3 - 10^5$ , depending on the stellar environment with respect to the kinematics of field stars and clusters. In addition, for typical planetesimal size distributions, a few of the captured objects could be  $\gtrsim$  km-sized.

Although the total mass captured is small compared to the dust abundance, the seeding of large planetesimals could catalyze planet formation in those discs and alleviate many of the problems involved in the formation of the first planetesimals, while overcoming the metre-size barrier. Perhaps similarly, there are also potential “second-generation” formation implications for objects embedded inside WD discs (Schleicher & Dreizler 2014; Völschow, Banerjee & Hessman 2014; Hogg, Wynn & Nixon 2018; van Lieshout et al. 2018).

In this paper, we estimate the rate and number of captured ISM planetesimals, exo-Kuiper belt and exo-Oort cloud objects in a WD planetary remnant debris disc. In Section 2, we describe our

assumptions of the WD gaseous disc properties. We derive the capture probabilities, rates and total number of captures in Section 3. Section 4 features loss cone dynamics for the exo-Oort cloud case. We discuss the implications in Section 5 and summarize in Section 6.

## 2 DISCS AROUND WHITE DWARFS

The lifetimes of WD debris discs are unknown. However, those can be estimated by dividing the the average mass of metals within the convection zone of DB WDs by the averaged accretion rates found in DA WDs. The result is  $3 \times 10^4 - 5 \times 10^6$  yr (Girven et al. 2012). Given the lifetimes of these discs and the tidal dissipation timescales, the amount of mass accreted by an embedded planetesimal is unknown.

The eight known WD debris discs which contain both gas and dust are kinematically constrained to have inner radii of about  $0.6R_{\odot}$  and outer radii of about  $1.2R_{\odot}$ . Their masses and size distributions are unknown, but between the inner rim and the WD photosphere any material transferred from the disc to the WD must be sublimated in the form of gas.

The structure of the gaseous components of WD discs has been explored by Metzger, Rafikov & Bochkarev (2012) and Kenyon & Bromley (2017b). Both sets of authors assume a constant arrival rate of solids onto the Roche radius and subsequent sublimation, but different temperature profile and  $\alpha$ -viscosity prescriptions. The solid component drifts inward due to Poynting-Robertson (PR) drag, while the gaseous component is spread out by viscous evolution. The inner region accreting directly onto the WD, while the outer region extends far beyond the Roche radius, up to  $\approx 20 R_{\odot}$ . In fact, the outward spreading is constrained only by the location at which solids recondense.

Both models predict a co-existent state of gas and debris, which is supported by observations (e.g. Gänsicke et al. 2006; Farihi 2016; Dennihy et al. 2018). It remains unclear why the gas does not condense back into solids beyond the sublimation point. van Lieshout et al. (2018) assumed that once the gas exceeds the Roche radius, it condenses to form minor planets. It is unclear why the unknown process that prevents condensation should be efficient only inside the Roche radius, namely where for optically thick discs the temperature is independent of the radius, as in Metzger, Rafikov & Bochkarev (2012). Here we assume a constant feeding rate, similarly to Metzger, Rafikov & Bochkarev (2012); Kenyon & Bromley (2017b), and that condensation is stalled also on larger scales and extend the gaseous disc much further away than the Roche radius.

### 2.1 Gaseous disc structure

We assume for simplicity that the WD gaseous discs extend from  $r_{\text{in}} = 8.7 \cdot 10^8$  cm to  $r_{\text{out}} = 1.4 \cdot 10^{12}$  cm  $\approx 20R_{\odot}$ , spanning three orders of magnitude. We normalize the surface density at  $r_0 \equiv 10^{10}$  cm, such that the surface density profile is

$$\Sigma_g(r) = \Sigma_{g,0} \left( \frac{r}{r_0} \right)^{-\beta} \quad (1)$$

where  $\beta$  is an arbitrary exponent. Metzger, Rafikov & Bochkarev (2012) find that  $\Sigma_g(r) \propto r^{-n-1/2}$ , where  $n$  describes the viscosity power law,  $\nu(r) \propto r^n$ . For a flat temperature profile,  $n = 3/2$ , and  $n = 1$  for optically thin disc with  $T(r) \propto r^{1/2}$ . We thus expect that  $\beta$  will be in the range of 1.5 – 2.0.

The total mass of the disc ( $\beta \neq 2$ ) is

$$M_{\text{disc}} = \int_{r_{\text{in}}}^{r_{\text{out}}} \Sigma_g(r) 2\pi r dr = 2\pi \Sigma_{g,0} r_0^\beta \int_{r_{\text{in}}}^{r_{\text{out}}} r^{1-\beta} dr \quad (2)$$

$$= \frac{2\pi}{2-\beta} \Sigma_{g,0} r_0^2 \left[ \left( \frac{r_{\text{out}}}{r_0} \right)^{2-\beta} - \left( \frac{r_{\text{in}}}{r_0} \right)^{2-\beta} \right]$$

For  $\beta < (>)2$  most of the mass is in the outer (inner) regions. In this case the total mass is determined by the outer (inner) boundary

$$M_{\text{disc}} \approx \frac{2\pi}{|2-\beta|} \Sigma_{g,0} r_0^2 \left( \frac{r_{\text{io}}}{r_0} \right)^{2-\beta}, \quad (3)$$

where  $r_{\text{io}}$  is the outer (inner) radius and  $\beta < (>)2$ .

For  $\beta = 2$ , each radial octave contributes the same amount of mass, and the total disc mass depends on the Coulomb logarithm  $\ln(r_{\text{in}}/r_{\text{out}})$  as

$$M_{\text{disc}} = 2\pi \Sigma_{g,0} r_0^2 \ln \left( \frac{r_{\text{out}}}{r_{\text{in}}} \right). \quad (4)$$

By inserting the fiducial values and taking  $M_{\text{disc}} = 10^{25}$  g with representative values of  $\beta$ , we have

$$\Sigma_{g,0} = 10^3 \text{ g cm}^{-2} \left( \frac{r_0}{10^{10} \text{ cm}} \right)^{-\beta} \left( \frac{M_{\text{disc}}}{10^{25} \text{ g}} \right) \begin{cases} 0.68 & \beta = 3/2 \\ 2.35 & \beta = 5/2 \\ 51 & \beta = 2 \end{cases} \quad (5)$$

To summarize, the typical normalization for a  $10^{25}$  g gas disc is  $\sim 10^3 - 10^4 \text{ g cm}^{-2}$ , regardless of the power-law density exponent  $\beta$ .

### 3 CAPTURE RATES

The capture rates of different populations of planetesimals depend both on the supply rate, and on the capture probability. For the ISM planetesimals, the supply rate is constant and depends mainly on the environment, while the capture probability is highly dependent on the size of the planetesimals and the disc structure. Conversely, exo-asteroid and exo-Oort objects are captured efficiently once they pass close enough to the disc, as long as they are not too massive. The supply rate, on the other hand, depends on the diffusion rate that brings new planetesimals into orbits that are lost, leading to the loss-cone dynamics presented in detail in sec. 4.

#### 3.1 ISM planetesimals

Consider a planetesimal of size  $R_p$  and density  $\rho_p$ , on a hyperbolic orbit with velocity at infinity  $v_\infty$  and impact parameter  $b$ , approaching a WD with mass  $M_{\text{WD}}$  and harbouring the gaseous disc structure that was described in sec. 2. A planetesimal passing through the disc loses energy due to aerodynamic gas drag. The most massive planetesimals could be decelerated by dynamical friction at lower relative velocities (Grishin & Perets 2015, 2016), but the initial capture occurs at high relative velocities, where dynamical friction is inefficient.

The planetesimal remains bound if the total loss energy is greater than its kinetic energy at infinity. Grishin, Perets & Avni (2019) found that this capture condition is

$$R_p \lesssim \frac{3}{4} \frac{C_D \Sigma_g(q)}{\rho_p} (1 + \Theta_s), \quad (6)$$

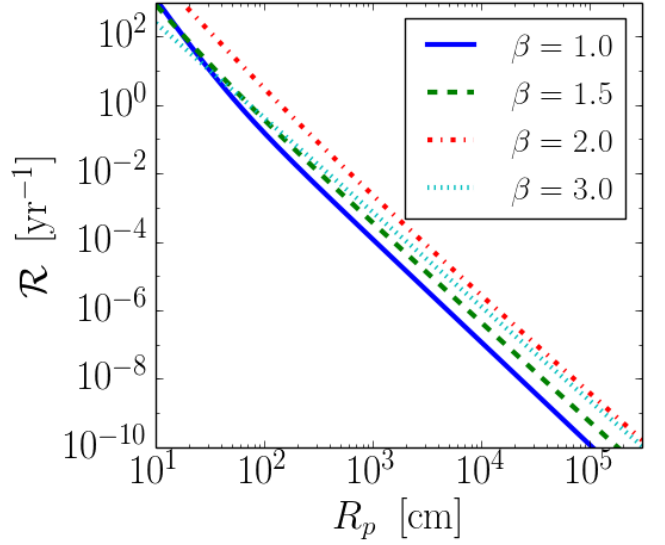


**Figure 1.** Total rates of interstellar objects embedded in the disc as a function of object size. Each line plots Eq. (10) with  $\alpha = 11/6$ ,  $f = 1$ ,  $M_{\text{WD}} = 0.6 M_\odot$ , and  $M_{\text{disc}} = 10^{25}$  g. The disc profile exponent is  $\beta = 1, 1.5, 2$  and  $3$  for the solid blue, dashed green, dot-dashed red and dotted cyan lines, respectively.

where  $C_D$  is the drag coefficient,  $\Theta_s \equiv v_{\text{esc}}^2/v_\infty^2$  is the gravitational focusing Safronov number and  $v_{\text{esc}}^2 = 2GM_{\text{WD}}/q \approx v_{\text{rel}}^2 - v_\infty^2$  is the escape velocity at closest approach  $q$ . For  $\Theta_s \gg 1$  gravitational focusing is important, while for  $\Theta_s \ll 1$  the scattering is mostly in the geometric collision regime.

By assuming that the velocities are distributed from a Maxwellian velocity distribution with dispersion  $\sigma$ , and the impact parameters are distributed from an area-uniform impact parameter distribution with cut-off  $b_{\text{max}}$ , Grishin, Perets & Avni (2019) found analytic expressions for the capture fractions as a function of the planetesimal's size and disc parameters. Although small pebbles are dominated by the geometric regime, large planetesimals are dominated by gravitational focusing. For the geometric regime, the capture probability is

$$f_c^{\text{geo}}(R_p) \approx \left( \frac{3C_D \Sigma_{g,0}}{4\rho_p R_p} \right)^{2/\beta} \left( \frac{b_{\text{max}}}{r_0} \right)^{-2}, \quad (7)$$

while for the gravitational focusing regime, the capture probability is

$$f_c^{\text{gf}}(R_p) = \Gamma(\beta') \left( \frac{3C_D \Sigma_{g,0}}{4\rho_p R_p} \right)^{\frac{1}{1+\beta}} \left( \frac{GM_{\text{WD}}}{\sigma^2 r_0} \right)^{\frac{2+\beta}{1+\beta}} \left( \frac{r_0}{b_{\text{max}}} \right)^2, \quad (8)$$

where  $\beta' = \beta/(1 + \beta)$ , and  $\Gamma(x)$  is the Gamma function.

Multiplying the capture probabilities (Eq. 7 and 8) by  $n_{\text{ISM}}(\sqrt{8/\pi}\sigma)\pi b_{\text{max}}^2$  gives the total capture rate. Here,  $n_{\text{ISM}}$  is the number density of ISM planetesimals of size less than  $R_p$ , which depends on the mass function and overall density. Here, we assume there is at least  $fM_\oplus$  mass in ejected planetesimals, where  $f = 1$ .

The number density of planetesimals is  $n_{\text{ISM}} = n_* N(R_p)$ , where  $n_* = 0.1 \text{ pc}^{-3}$  is the stellar number density in the field and  $N(m)$  is the number of planetesimals of mass  $\leq m$ , which are estimated as follows: The mass function is likely to follow a power law distribution,  $dN/dm \propto m^{-\alpha}$ . Small bodies are likely

to follow collisional (Dohnanyi) distribution, (Dohnanyi 1969) i.e.  $dN/dm \propto m^{-11/6}$ , while large bodies could be formed by streaming instability, i.e.  $dN/dm \propto m^{-5/3}$ . We leave the mass function exponent  $\alpha$  as a free parameter. The number of planetesimals is (Grishin, Perets & Avni 2019)

$$N(m) = \frac{2 - \alpha}{\alpha - 1} 10^{2-\alpha} f \left( \frac{R_p}{R_\oplus} \right)^{3-3\alpha}, \quad (9)$$

where  $R_\oplus$  is Earth's radius. In Eq. (9) we assumed that the largest ejected planetesimal mass is  $0.1M_\oplus$ .

The total capture rates are thus

$$\mathcal{R}(R_p) = \frac{2 - \alpha}{\alpha - 1} 10^{2-\alpha} \sqrt{8\pi} f \left( \frac{R_p}{R_\oplus} \right)^{3-3\alpha} K(R_p) n_* \sigma r_0^2, \quad (10)$$

where

$$K(R_p) \equiv \begin{cases} \left( \frac{3C_D \Sigma_{g,0}}{4\rho_p R_p} \right)^{2/\beta} & \text{geo} \\ \Gamma \left( \frac{\beta}{1+\beta} \right) \left( \frac{3C_D \Sigma_{g,0}}{4\rho_p R_p} \right)^{1/(1+\beta)} \left( \frac{GM_{\text{WD}}}{\sigma^2 r_0} \right)^{\frac{2+\beta}{1+\beta}} & \text{gf} \end{cases} \quad (11)$$

Figure 1 shows the total disc-embedding rates obtained by Eq. (10). The typical values are of a system of a WD of mass  $M_{\text{WD}} = 0.6M_\odot$ , and a total mass of the disc  $M_{\text{disc}} = 10^{25}$  g with surface density profile exponent  $\beta$  as a free parameter. The normalized surface density  $\Sigma_{g,0}$  is set from Eq. (5) in sec. 2.1. The solid density is set to  $\rho_p = 1 \text{ g cm}^{-3}$ .

The total mass capture rate scales as  $\sim \mathcal{R} \rho_p R_p^3$ , and ranges around  $10^{-4} - 10^{-2} \text{ g s}^{-1}$ , around 10 orders of magnitude less than the inferred metal pollution rate of  $\sim 10^8 \text{ gs}^{-1}$ . Thus, ISM capture cannot be the source of metal pollution on WDs, as expected. Nevertheless, the captured ISM material could play a role in the overall disc evolution, similarly to protoplanetary discs. In addition, the frequent capture of cm-sized pebbles may provide observational signatures.

### 3.2 Exo-Kuiper belt objects and exo-Oort cloud comets

Consider now a body of size  $R_p$ , and density  $\rho_p$ , but on a bound orbit with semi-major axis  $a$  and eccentricity  $e$ . The pericentre distance is  $q = a(1 - e)$ . During the passage through the gaseous disc, most of the energy loss occurs near pericentre. Hence, the energy loss is (Grishin, Perets & Avni 2019)

$$\Delta E = -\frac{\pi}{2} C_D R_p^2 \Sigma_g(q) v_{\text{rel}}^2. \quad (12)$$

For a highly eccentric orbit, the velocity is approximated by the escape velocity  $v_{\text{rel}}^2 = 2GM_{\text{WD}}/q$ , and thus the energy loss is

$$\Delta E = -\pi C_D GM_{\text{WD}} R_p^2 \frac{\Sigma_g(q)}{q}. \quad (13)$$

Since the orbital energy  $E_{\text{orb}} = -GM_{\text{WD}} m_p / 2a$  is small, the ratio between the dissipated energy and orbital energy, namely

$$\left| \frac{\Delta E}{E_{\text{orb}}} \right| = \frac{3C_D \Sigma_g(q) a}{2\rho_p R_p q}, \quad (14)$$

is small for very eccentric orbits. The body will be circularized and embedded in the gaseous disc within an orbital timescale if  $R_p \lesssim (a/q) \Sigma_g / \rho_p$ . This relation is definitely true for all Oort-cloud objects with extreme ratios of  $a/q \gtrsim 10^8$ , and is true for exo-Kuiper Belt objects under  $\lesssim 1 \text{ km}$  in size, where  $a/q \approx 10^4$ .

For massive planetesimals and less massive gaseous disc (but

much more massive than the planetesimals' mass,  $M_{\text{disc}} \gg \rho_p R_p^3$ ), the orbital energy will be dissipated only after several orbital cycles. The energy dissipation time can be defined as  $\tau_E \equiv E_{\text{orb}} / (dE/dt)$ , where  $dE/dt = \Delta E / P_{\text{orb}}$ , with  $P_{\text{orb}}$  being the orbital time of the body around the WD. The dissipation time is then

$$\begin{aligned} \tau_E &= \frac{E_{\text{orb}}}{dE/dt} = \frac{GM_{\text{WD}} m_p}{2a} \frac{2\pi}{\Delta E} \sqrt{\frac{a^3}{GM_{\text{WD}}}} \\ &= \frac{q}{v_K(a)} \frac{4\pi \rho_p R_p}{3C_D \Sigma_g(q)}, \end{aligned} \quad (15)$$

where  $v_K(a) \equiv (GM_{\text{WD}}/a)^{1/2}$  is the Keplerian velocity of a circular orbit at semimajor axis  $a$ .

Figure 2 shows the dissipation times for exo-Kuiper Belt object orbits and exo-Oort type orbits. The initial semimajor axes are 40 au for exo-Kuiper Belt object orbits and  $10^4$  au for exo-Oort cloud orbits. The pericentre is either  $q = R_\odot$  (left panels) or  $q = 15R_\odot$  (right panels). In order to compute the timescale, for each value of  $R_p$  we plot the maximum of the orbital time and  $\tau_E$  from Eq. (15). We display the results for relatively low mass gaseous discs  $M_{\text{disc}} = 10^{23}$  g (top panels) and a gaseous disc of mass  $M_{\text{disc}} = 10^{25}$  g (bottom panels). Even for the lower mass disc, the dissipation times extend beyond the orbital periods only for large objects.

Therefore, the flat regions of the curves in Fig. 2 reveal that most Oort-cloud planetesimals are captured within one orbital period. For extremely low-mass discs and orbital pericenters of  $15R_\odot$ , planetesimals smaller than 0.1(10) km are captured in one orbit in a  $10^{23}(10^{25})$  g disc. Although larger objects are captured after longer times, the dissipation timescales are typically short relative to the orbital period. Thus, the capture rate mostly depends on the supply rate of Oort-cloud planetesimals into low angular momentum orbits, which is the main focus of the next section.

## 4 LOSS CONE DYNAMICS FOR EXO-OORT CLOUDS

Due to the short dissipation timescales, planetesimals on low angular momentum (high- $e$ ) orbits are captured within one orbital time and effectively ‘‘lost’’. Therefore the capture rate is dominated by the flux of planetesimals into high- $e$  orbits, which is generally dominated by collective diffusive processes. The high- $e$  (low angular momentum) orbits which are captured form the shape of a cone in action space. Therefore, the dynamical origins of the supply rate into high- $e$  orbits is denoted ‘loss cone dynamics’ (see Merritt 2013 for a review).

Loss cone dynamics are determined by two parameters (or times): The critical angular momentum required for loss,  $J_c$  and the average change in the angular momentum within one orbit,  $\Delta J$ . If the change is small, then  $|\Delta J| \ll J_c$ , the replenishment time is longer than the orbital period, and the cone is mostly empty. This case corresponds to the empty loss cone regime and the loss rate is determined by the replenishment rate. Conversely, if the change in the angular momentum per orbit is large, then  $|\Delta J| \gtrsim J_c$ , the replenishment time is much faster, and the loss rate is determined by the removal time. Here, the cone is mostly full: this situation corresponds to the full loss cone regime.

The drivers for the diffusive flux rate of exo-asteroids and exo-Oort cloud planetesimals are very different. Exo-asteroid diffusion rates are highly sensitive to the architecture of a planetary system and the details of its destabilization. Given the variations between the number of, mass of and mutual distances between exo-planets

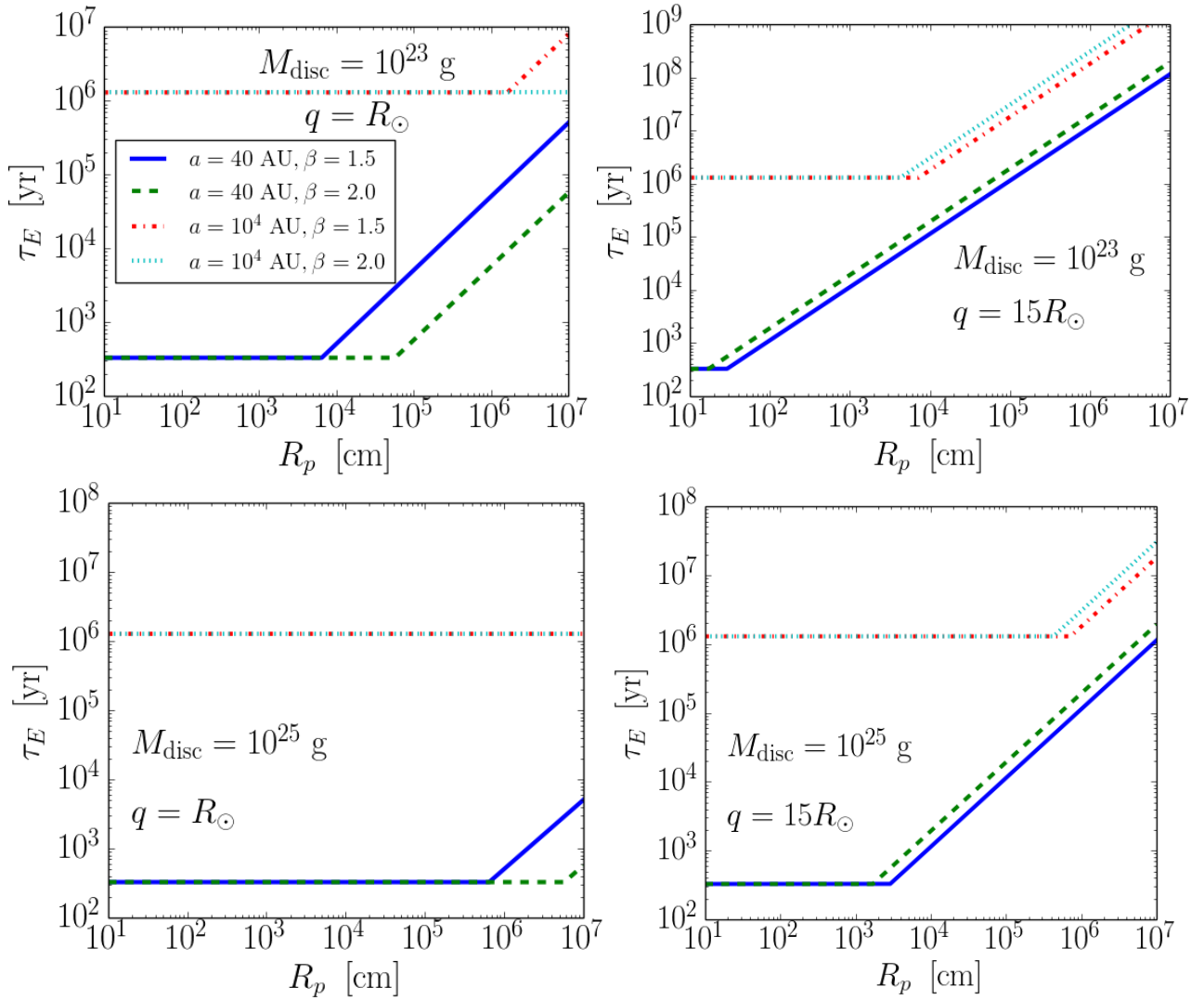


**Figure 2.** Dissipation times (times to achieve final orbit) of bound exo-Kuiper Belt objects and exo-Oort cloud objects. Each line plots the maximum of the orbital period and Eq. (15) with  $M_{\text{WD}} = 0.6M_{\odot}$ . Top panels show discs of mass  $M_{\text{disc}} = 10^{23}$  g, while bottom panels have more massive discs with  $M_{\text{disc}} = 10^{25}$  g. Left panels show an orbital pericentre of  $q = R_{\odot}$ , while the right panels show a larger pericentre of  $q = 15R_{\odot}$ . In each panel the disc profile exponent is  $\beta = 1.5$  for Kuiper Belt object orbits (solid blue line) and Oort cloud orbits (dot-dashed red line), and  $\beta = 2$  for Kuiper Belt object orbits (dashed green line) and Oort cloud orbits (dotted cyan line).

in separate systems, obtaining an analytical description of the loss cone regime for exo-asteroids across all systems is not yet feasible.

However, the situation is more optimistic for exo-Oort cloud comets because their diffusive flux rate is dominated by Galactic tides (Heisler & Tremaine 1986). Encounters of molecular clouds enhance the Oort cloud evolution and accretion rate (Wickramasinghe, & Napier 2008). Similar processes occur in the Galactic centre, with various types of relaxation, as well as massive perturbers and spiral-arms (Perets et al. 2007; Hamers & Perets 2017).

In order to estimate the rate of captured exo-Oort cloud objects, we use the loss cone flux derived by Heisler & Tremaine (1986). The time to capture the planetesimals is bounded from above by the orbital time ( $\sim 10^6$  yr), while the replenishment time is on the order of Gyr. Therefore, we use the expression for the empty loss cone regime.

For a comet at semimajor axis  $a$  and eccentricity  $e$ , the canonical actions are  $L = \sqrt{\mu a}$ ,  $J = \sqrt{\mu a(1 - e^2)}$  with  $\mu \equiv GM_{\text{WD}}$ . For large enough semimajor axis  $a$ , Galactic tides are fast enough to

perturb the orbits into very large eccentricity (but still much slower than the orbital period, hence the empty loss cone assumption is maintained) and pericentre  $q = a(1 - e) \ll a$ , which results in changing the action to  $J_q \approx \sqrt{2\mu q}$ . For a critical pericenter  $q_c$ , orbits with  $J_q \leq J_c = \sqrt{2\mu q_c}$  are destroyed. If  $f_{\text{DF}}(L, J)$  is the distribution function; namely that the number of Oort cloud comets in the action phase  $dLdJ$  is  $dN = f_{\text{DF}}(L, J)dLdJ$ , Heisler & Tremaine (1986) find that the flux per unit  $L$  is:

$$F_{\text{empty}}(L) = f_{\text{DF}}(L, J) \frac{160\pi^3 G \rho_0}{3\mu^2} J_q L^4, \quad (16)$$

where  $\rho_0 = 0.185M_{\odot}\text{pc}^{-3}$  is the local density. The transition to the empty loss cone occurs at  $a \lesssim 10^4$  au, a region which we assume to be devoid of planetesimals. Thus in our case the loss cone is always empty.

#### 4.1 Distribution function and rates

Here we obtain an explicit distribution function and use it to calculate the loss rates of Oort cloud comets.

We assume for simplicity that the distributions of the semimajor axis and the eccentricity are uniform, independent of each other, and are represented by power-laws as:

$$f_A(a) = k_a a^{-p}; f_E(e) = 1 \quad (17)$$

where the domains are  $a \in [a_{\min}, a_{\max}]$ ;  $e \in [0, 1)$ . The normalization is related to the distribution by  $1 = \int_{a_{\min}}^{a_{\max}} f(a) da = 1$ . For  $p \neq 1$  we have

$$k_a = \frac{1-p}{a_{\max}^{1-p} - a_{\min}^{1-p}} \quad (18)$$

while  $k_a = 1/\ln(a_{\max}/a_{\min})$  for  $p = 1$ .

If the joint distribution of  $a$  and  $e$  is independent, i.e.  $f_{\text{joint}}(a, e) = f_A(a)f_E(e)$ , then the number of comets is

$$dN = N_{\text{tot}} f_A(a) f_E(e) = f_{\text{DF}}(L, J) dL dJ. \quad (19)$$

Thus, the distribution function is given by the Jacobian transformation (the off-diagonal terms vanish since  $\frac{\partial L}{\partial e} = \frac{\partial a}{\partial J} = 0$ )

$$f_{\text{DF}}(L, J) = N_{\text{tot}} f_A(a) f_E(e) \left| \frac{\partial a}{\partial L} \frac{\partial e}{\partial J} \right|.$$

By inverting the relations, we obtain  $a = L^2/\mu$  and  $e = 1 - J^2/L^2$ . The derivatives are

$$\frac{\partial a}{\partial L} = \frac{2L}{\mu}; \quad \frac{\partial e}{\partial J} = -2 \frac{J}{L^2}$$

yielding

$$\begin{aligned} f_{\text{DF}}(L, J) &= 4 \frac{N_{\text{tot}}}{\mu} k_a a(L)^{-p} \frac{J}{L} \\ &= 4 \mu^{p-1} N_{\text{tot}} k_a \frac{J}{L^{2p+1}}. \end{aligned} \quad (20)$$

It can be verified that the number of comets is retained, namely  $N_{\text{tot}} = \int_{L_{\min}}^{L_{\max}} \int_0^{J_{\max}(L)} f_{\text{DF}}(L, J) dJ dL$ .

For the empty loss case, by using Eqns (16) and (20), we find that the empty loss cone rate is

$$F(L) = \frac{640\pi^3 G \rho_0}{3} \mu^{p-3} N_{\text{tot}} k_a J_q^2 L^{3-2p}. \quad (21)$$

Note that  $F(L)$  is independent of  $L$  if  $p = 3/2$ . After plugging in, e.g.  $p = 3/2$ ,  $a_{\text{in}} = 10^4 \text{ au}$  and  $a_{\text{out}} = 10^5 \text{ au}$ ,  $N_{\text{tot}} = 10^9$ ,  $q = R_{\odot}$ , we obtain

$$F(L) = 7.8 \cdot 10^{-3} \left( \frac{q}{R_{\odot}} \right) \left( \frac{N_{\text{tot}}}{10^9} \right) \left( \frac{a_{\max}}{10^5 \text{ AU}} \right)^{1/2} \text{ yr}^{-1}. \quad (22)$$

#### 4.2 Size-dependent rate

In deriving Eq. (22) we assumed that all comets have a single mass. In general, however, the comets are described by a mass function  $dN/dm \propto m^{-l}$ . The overall number of comets with mass  $m$  is (Grishin, Perets & Avni 2019)

$$N(m) = \frac{2-l}{l-1} \frac{M_{\text{tot}}}{m^{l-1} m_{\text{up}}^{2-l}}$$

where  $1 > l > 2$ .

For a collisional distribution (Dohnanyi 1969),  $l = 11/6$ , total mass of  $M_{\text{tot}} = 10^{28} \text{ g}$ , and the largest body has a mass of

$m_{\text{up}} \approx 10^{21} \text{ g}$ , which corresponds to a  $\sim 100 \text{ km}$  planetesimal, We have

$$N(m) = 2 \cdot 10^7 \left( \frac{m}{10^{21} \text{ g}} \right)^{-5/6}.$$

For the size dependence, we use  $m = 4\pi\rho_p R_p^3/3$  to obtain, for  $\rho_p = 1 \text{ g cm}^{-3}$ ,

$$N(R_p) = 6 \cdot 10^6 \left( \frac{R_p}{100 \text{ km}} \right)^{-5/2}.$$

Finally, for the empty loss cone regime, we obtain the size-dependent analog to equation (22)

$$F(L, R_p) = 1.4 \cdot 10^{-2} \left( \frac{R_p}{10 \text{ km}} \right)^{-5/2} \left( \frac{q}{R_{\odot}} \right) \left( \frac{a_{\max}}{10^5 \text{ AU}} \right)^{1/2} \text{ yr}^{-1}. \quad (23)$$

The total captured mass rate is

$$\frac{dm}{dt} = \int_{R_p=0 \text{ km}}^{100 \text{ km}} 4\pi R_p^2 \rho_p F(R_p) dR_p \approx 10^{18} \text{ g yr}^{-1}. \quad (24)$$

For the assumed Oort-cloud mass of  $M_{\text{tot}} = 10^{28} \text{ g}$ , up to 10 per cent of the mass could be captured within 1 Gyr for  $q = R_{\odot}$ , whereas numerical simulations show that  $\sim 10^{-5}$  of the mass is disrupted, the analytical calculation of Alcock, Fristrom & Siegelman (1986) finds that  $\sim 1\%$  of the objects are disrupted.

The latter is only an averaged estimate and depends on many parameters. The number density of the cloud reduces over time. In addition, the Galactic tide works over  $\sim \text{Gyr}$  timescales, while comets have taken their new orbits only after stellar mass loss and the birth of the WD. Moreover, the furthest away planetesimals will be depleted first. Therefore, the maximal excursion will also change over time.

Regardless of the uncertainties, the calculated rates are comparable and provide an analytic framework to estimate the order of magnitudes. In addition, the loss rate depends linearly on the critical pericenter,  $q_c$ . Thus, extended gaseous discs far beyond the Roche limit,  $r_{\text{out}} \gg R_{\odot}$ , will capture planetesimals by a factor  $r_{\text{out}}/R_{\odot}$  higher than the number of planetesimals which are disrupted, regardless of their sizes and disc properties (up to some limit). In our case of an outer WD radius up to  $20R_{\odot}$ , the embedded mass could be  $\sim 20$  times the mass of the disrupted planetesimals, significantly altering the gas-to-dust ratio of the disc.

## 5 DISCUSSION

Our results potentially have implications for all WD planetary debris discs, not just the ones with embedded planetesimals. The pebbles and boulders captured change the size distribution of the debris disc, with implications for both modelling and observations. From the modelling perspective, a time-dependent size distribution and steady, periodic or intermittent inflow of material should be incorporated into simulations; a collisional cascade code like that used by Kenyon & Bromley (2017a,b) can accomplish this task.

From the observational perspective, there is increasing evidence of WD debris discs showcasing variability on the per cent to tens of per cent level on yearly timescales (Gänsicke et al. 2008; Wilson et al. 2014; Xu & Jura 2014; Farihi et al. 2018; Xu et al. 2018; Swan et al. 2019). Not all these discs have observable gas, although it might be present anyway (Bonsor et al. 2017). Flux

changes over yearly or decadal timescales may be the result of changing size distributions and orbital shifting within those discs. Attempting to reproduce these changes in a particular system due to small-body capture represent enticing challenges for dedicated future studies.

One particularly interesting result of our investigations is that for sufficiently extended gaseous discs, capture is more likely than disruption (see end of Section 4). Consequently, there are implications for how debris discs are recycled on timescales much longer than the  $\sim$  Myr upper bound suggested by [Girven et al. \(2012\)](#). There are several important consequences. The first is a new source-sink relationship between the dust and the gas in the disc. Another are the geometric signatures resulting from a captured planetesimal ([Manser et al. 2019](#)). A third is the possibility of capture of multiple large planetesimals which could gravitationally perturb one another as well as the disc. A fourth is captured objects which could reside close to the locations where second-generation planetesimals may form from a massive disc ([van Lieshout et al. 2018](#)).

We assumed a fixed gaseous disc mass (except in Section 3.2). The ISM planetesimals have a large (positive) energy, therefore their capture rate depends both on their orbits and on the gaseous disc properties. The capture rate of ISM planetesimals has a shallow dependence on the gaseous disc mass and surface density profile (see Eq. 11). Loosely bound exo-KBO and exo-Oort orbits have low orbital energy, and generally their energy dissipation time is shorter than their long orbital time (see Fig. 2), therefore for most cases their capture rate is independent of the disc mass and determined by the replenishment rate of new exo-KBO and exo-Oort comets into loss cone orbits, up to the point where there is not enough mass to capture the planetesimal within one passage (see Fig. 2).

Our key assumption is that the gaseous disc is extended beyond the Roche limit, and that there is a co-existent state of gas and solids (see Section 2). The co-existent state is supported both by theory and observations, while the large radial extent is supported by theory, but currently not observed. Future observations should confirm or falsify our assumptions, and a deeper understanding of the physical mechanisms that permit the co-existent state is still lacking. By truncating the disc extent to the Roche limit, the planetesimals will be disrupted rather than captured. Capture would be possible only for compact planetesimals with high internal strength, which could provide the origin of the planetary core orbiting SDSS J1288+1040 ([Manser et al. 2019](#)) well within the Roche limit.

There is increasing evidence that just about all metal pollution arises from disc accretion, regardless if the discs can be seen ([Bergfors et al. 2014](#); [Farihi 2016](#); [Bonsor et al. 2017](#)). The gaseous components of the disc can enhance the supply rate of solids that eventually form the debris component of the disc. The link between the chemical composition of the embedded seed and the eventual abundances measured in the white dwarf atmosphere is tenuous due to seed's acquisition of solids, chemical mixing with the existing disc, and subsequent fragmentation before accretion onto the white dwarf.

The chemical composition of the existing discs themselves ([Reach et al. 2005, 2009](#)) are produced from the destruction of minor planets. Although these minor planets are predominantly dry ([Jura & Young 2014](#); [Hollands, Gänsicke & Koester 2018](#)), in contrast [Xu et al. \(2017\)](#) discovered a volatile-rich metal polluted WD with a nitrogen mass fraction comparable to that of comet Halley and higher than that of any inner solar system object. This metal polluted WD also contains significant fractions of other

volatiles like carbon which are more characteristic of cometary objects than terrestrial rocky objects. Combined with the water-rich progenitor minor planets in a few other WD systems ([Farihi et al. 2013](#); [Raddi et al. 2015](#); [Gentile Fusillo et al. 2017](#)), the volatile-rich object from [Xu et al. \(2017\)](#) suggests that multiple reservoirs supply WDs with metal pollutants. Water retention in minor planets is possible throughout the giant branch stages of stellar evolution ([Malamud, & Perets 2016, 2017a,b](#)).

Finally, our numerical results are subject to the usual caveats of the currently unconstrained nature of architectures of WD planetary systems and the unknown disc lifetimes. However, we deliberately have kept our formalism general enough to allow the reader to insert their favoured distributions, rates and orbits into the equations.

## 6 SUMMARY

The dynamic environment close to WDs is strongly influenced by external factors, with incoming exo-planetesimals representing frequent interlopers. After one of them disrupts at the WD Roche radius and forms a disc, the outward spread of the resulting gas allows new exo-planetesimals with orbital pericentres outside of the Roche radius to interact with the disc without being destroyed.

Sometimes this interaction leads to direct capture, representing the scenario we study here. Enabling this work is the analytical formalism developed by [Grishin, Perets & Avni \(2019\)](#), which ultimately led to explicit expressions for capture rates of interstellar planetesimals (equation 10) and orbital dissipation timescales for the already-bound orbits of exo-Kuiper belts and exo-Oort cloud comets (equation 15). Estimating the fraction of exo-Kuiper belt objects which are on capture orbits is currently too unconstrained to be analytically characterised. However, this fraction may be computed for exo-Oort cloud comets (equation 23) by using the supply rate from Galactic tides ([Heisler & Tremaine 1986](#)). These equations are general enough to be applied to most white dwarf planetary systems with discs.

We found that capture of interstellar objects into white dwarf discs is negligible, but capture from (already bound) exo-Kuiper belt and exo-Oort cloud objects is important. In an extended gaseous disc of  $\sim 20R_{\odot}$  capture is  $\sim 20$  times more likely than disruption. The probability of capture scales strongly with planetesimal size, and there is a nonzero probability that the planetary core fragment embedded with the SDSS J1288+1040 disc was captured by the gaseous component of that disc. Besides minor planets which are at least a km in size, capture of much smaller m- and cm-size particles like boulders and pebbles is likely to provide a continuously changing size distribution in the discs. Capture on yearly or decadal timescales might even explain variability which is seen in some WD discs.

## ACKNOWLEDGEMENTS

We thank the referee for their useful feedback, which has improved the manuscript. Both EG and DV acknowledge useful discussions at the Lorentz Workshop *Trendy-2* which has led to this result. We also thank Brian David Metzger and Roman Rafikov for helpful correspondence. EG acknowledges support by the Technion Irwin and Joan Jacobs Excellence Fellowship for outstanding graduate students. DV gratefully acknowledges the support of the STFC via an Ernest Rutherford Fellowship (grant ST/P003850/1).

## REFERENCES

- Adams F. C., Bloch A. M., 2013, *ApJ*, 777, L30
- Alcock C., Frstrom C. C., Siegelman R., 1986, *ApJ*, 302, 462
- Bear E., Soker N., 2013, *NewA*, 19, 56
- Bergfors, C., Farihi, J., Dufour, P., & Rocchetto, M. 2014, *MNRAS*, 444, 2147
- Bochkarev K. V., Rafikov R. R., 2011, *ApJ*, 741, 36
- Bonsor A., Mustill A. J., Wyatt M. C., 2011, *MNRAS*, 414, 930
- Bonsor, A., Farihi, J., Wyatt, M. C., & van Lieshout, R. 2017, *MNRAS*, 468, 154
- Brown, J. C., Veras, D., & Gänsicke, B. T. 2017, *MNRAS*, 468, 1575
- Caiazzo I., Heyl J. S., 2017, *MNRAS*, 469, 2750
- Cauley, P. W., Farihi, J., Redfield, S., Bachman, S., Parsons, S. G., Gänsicke, B. T. 2018, *ApJL*, 852, L22
- Debes J. H., Walsh K. J., Stark C., 2012, *ApJ*, 747, 148
- Dennihiy, E., Clemens, J. C., Dunlap, B. H., et al. 2018, *ApJ*, 854, 40
- Dohnanyi J. S., *J. Geophys. Res.*, 74, 2531
- Farihi, J., Gänsicke, B. T., & Koester, D. 2013, *Science*, 342, 218
- Farihi, J. 2016, *New Astronomy*, 71, 9
- Farihi, J., van Lieshout, R., Cauley, P. W., et al. 2018, *MNRAS*, 481, 2601.
- Frewen S. F. N., Hansen B. M. S., 2014, *MNRAS*, 439, 2442
- Gallet F., Bolmont E., Mathis S., Charbonnel C., Amard L., 2017, *A&A*, 604, A112
- Gänsicke, B. T., Marsh, T. R., Southworth, J., & Rebassa-Mansergas, A. 2006, *Science*, 314, 1908
- Gänsicke, B. T., Koester, D., Marsh, T. R., Rebassa-Mansergas, A., & Southworth, J. 2008, *MNRAS*, 391, L103
- Gänsicke B. T., Koester D., Farihi J., Girven J., Parsons S. G., Breedt E., 2012, *MNRAS*, 424, 333
- Gänsicke, B. T., Aungwerojwit, A., Marsh, T. R., et al. 2016, *ApJL*, 818, L7
- Gary, B. L., Rappaport, S., Kaye, T. G., Alonso, R., & Hamschs, F.-J. 2017, *MNRAS*, 465, 3267
- Gentile Fusillo, N. P., Gänsicke, B. T., Farihi, J., et al. 2017, *MNRAS*, 468, 971
- Girven J., Brinkworth C. S., Farihi J., Gänsicke B. T., Hoard D. W., Marsh T. R., Koester D., 2012, *ApJ*, 749, 154
- Graham J. R., Matthews K., Neugebauer G., Soifer B. T., 1990, *ApJ*, 357, 216
- Grishin E., Perets H. B., 2015, *ApJ*, 811, 54
- Grishin E., Perets H. B., 2016, *ApJ*, 820, 106
- Grishin E., Perets H. B., Avni Y., 2019, *MNRAS* 487, 3324
- Gurri, P., Veras, D., & Gänsicke, B. T. 2017, *MNRAS*, 464, 321
- Hamers, A. S., & Perets, H. B. 2017, *ApJ*, 846, 123
- Hamers A. S., Portegies Zwart S. F., 2016, *MNRAS*, 462, L84
- Harrison J. H. D., Bonsor A., Madhusudhan N., 2018, *MNRAS*, 479, 3814
- Heisler J., Tremaine S., 1986, *Icarus*, 65, 13
- Hogg M. A., Wynn G. A., Nixon C., 2018, *MNRAS*, 479, 4486
- Hollands M. A., Gänsicke B. T., Koester D., 2018, *MNRAS*, 477, 93
- Izquierdo, P., Rodríguez-Gil, P., Gänsicke, B. T., et al. 2018, *MNRAS*, 481, 703
- Jura M., 2003, *ApJ*, 584, L91
- Jura M., Young E. D., 2014, *AREPS*, 42, 45
- Kenyon, S. J., & Bromley, B. C. 2017a, *ApJ*, 844, 116
- Kenyon, S. J., & Bromley, B. C. 2017b, *ApJ*, 850, 50
- Madappatt, N., De Marco, O., & Villaver, E. 2016, *MNRAS*, 463, 1040.
- Malamud, U., & Perets, H. B. 2016, *ApJ*, 832, 160
- Malamud, U., & Perets, H. B. 2017a, *ApJ*, 842, 67
- Malamud, U., & Perets, H. B. 2017b, *ApJ*, 849, 8
- Manser, C. J., Gänsicke, B. T., Marsh, T. R., et al. 2016, *MNRAS*, 455, 4467
- Manser, C. J., Gänsicke, B. T. et al. 2019, *Science*, 364, 66
- Meech, K. J., Weryk, R., Micheli, M., et al. 2017, *Nature*, 552, 378
- Merritt D., 2013, *CQGra*, 30, 244005
- Metzger, B. D., Rafikov, R. R., & Bochkarev, K. V. 2012, *MNRAS*, 423, 505
- Miranda, R., & Rafikov, R. R. 2018, *ApJ*, 857, 135
- Mustill A. J., Villaver E., Veras D., Gänsicke B. T., Bonsor A., 2018, *MNRAS*, 476, 3939
- Mustill A. J., Villaver E., 2012, *ApJ*, 761, 121
- Nordhaus J., Spiegel D. S., 2013, *MNRAS*, 432, 500
- Payne M. J., Veras D., Gänsicke B. T., Holman M. J., 2017, *MNRAS*, 464, 2557
- Perets, H. B., Hopman, C., & Alexander, T. 2007, *ApJ*, 656, 709
- Petrovich C., Muñoz D. J., 2017, *ApJ*, 834, 116
- Raddi, R., Gänsicke, B. T., Koester, D., et al. 2015, *MNRAS*, 450, 2083
- Rafikov, R. R. 2011a, *MNRAS*, 416, L55
- Rafikov, R. R. 2011b, *ApJL*, 732, L3
- Rafikov, R. R., & Garmilla, J. A. 2012, *ApJ*, 760, 123
- Rao, S., Meynet, G., Eggenberger, P., et al. 2018, *A&A*, 618, A18.
- Rappaport, S., Gary, B. L., Kaye, T., Vanderburg, A., Croll, B., Benni, P., Foote, J. 2016, *MNRAS*, 458, 3904
- Reach, W. T., Kuchner, M. J., von Hippel, T., et al. 2005, *ApJL*, 635, L161
- Reach W. T., Lisse C., von Hippel T., Mullally F., 2009, *ApJ*, 693, 697
- Redfield, S., Farihi, J., Cauley, P. W., Parsons, Steven G., Gänsicke, B. T., Duvvuri, G. M. 2017, *ApJ*, 839, 42
- Schleicher D. R. G., Dreizler S., 2014, *A&A*, 563, A61
- Smallwood J. L., Martin R. G., Livio M., Lubow S. H., 2018, *MNRAS*, 480, 57
- Stephan A. P., Naoz S., Zuckerman B., 2017, *ApJ*, 844, L16
- Stone N., Metzger B. D., Loeb A., 2015, *MNRAS*, 448, 188
- Sun, M., Arras, P., Weinberg, N. N., et al. 2018, *MNRAS*, 481, 4077.
- Swan, A., Farihi, J., & Wilson, T. G. 2019, *MNRAS*, 484, L109.
- van Lieshout R., Kral Q., Charnoz S., Wyatt M. C., Shannon A., 2018, *MNRAS*, 480, 2784
- Vanderburg, A., Johnson, J. A., Rappaport, S., et al. 2015, *Nature*, 526, 546
- Vanderburg, A., & Rappaport, S. A. 2018, *arXiv:1804.01997*
- Veras, D., Leinhardt, Z. M., Bonsor, A., & Gänsicke, B. T. 2014a, *MNRAS*, 445, 2244
- Veras D., Shannon A., Gänsicke B. T., 2014b, *MNRAS*, 445, 4175
- Veras, D., Leinhardt, Z. M., Eggl, S., & Gänsicke, B. T. 2015a, *MNRAS*, 451, 3453
- Veras D., Eggl S., Gänsicke B. T., 2015b, *MNRAS*, 452, 1945
- Veras D., 2016, *Royal Society Open Science*, 3, 150571
- Veras, D., Marsh, T. R., & Gänsicke, B. T. 2016b, *MNRAS*, 461, 1413
- Veras, D., Mustill, A. J., Gänsicke, B. T., et al. 2016a, *MNRAS*, 458, 3942
- Veras, D., Carter, P. J., Leinhardt, Z. M., & Gänsicke, B. T. 2017, *MNRAS*, 465, 1008
- Veras, D., Xu, S., & Rebassa-Mansergas, A. 2018, *MNRAS*, 473, 2871
- Villaver E., Livio M., Mustill A. J., Siess L., 2014, *ApJ*, 794, 3
- Völschow M., Banerjee R., Hessman F. V., 2014, *A&A*, 562, A19
- Wickramasinghe, J. T., & Napier, W. M. 2008, *MNRAS*, 387, 153
- Wilson, D. J., Gänsicke, B. T., Koester, D., Raddi, R., Breedt, E., Southworth, J., Parsons, S. G. 2014, *MNRAS*, 445, 1878
- Wyatt, M. C., Farihi, J., Pringle, J. E., & Bonsor, A. 2014, *MNRAS*, 439, 3371
- Xu, S., & Jura, M. 2014, *ApJL*, 792, L39
- Xu, S., Zuckerman, B., Dufour, P., et al. 2017, *ApJL*, 836, L7
- Xu, S., Su, K. Y. L., Rogers, L. K., et al. 2018, *ApJ*, 866, 108.

This paper has been typeset from a  $\text{\TeX}/\text{\LaTeX}$  file prepared by the author.